

# Estimating the Lensing Probability for Binary Black Hole Mergers in AGN disk by Using Mismatch Threshold

Wen-Long Xu,<sup>1</sup> Yu-Zhe Li,<sup>1</sup> Yi-Gu Chen,<sup>1</sup> Hui Li,<sup>2, a</sup> and Wei-Hua Lei<sup>1, b</sup>

<sup>1</sup>*Department of Astronomy, School of Physics, Huazhong University of Science and Technology, Luoyu Road 1037, Wuhan, 430074, China*

<sup>2</sup>*Theoretical Division, Los Alamos National Laboratory, Los Alamos, NM 87545, USA*

(Dated: June 13, 2025)

Stellar-mass binary black holes (BBH) may form, evolve, and merge within the dense environments of active galactic nuclei (AGN) disks, thereby contributing to the BBH population detected by gravitational wave (GW) observatories. Mergers occurring in AGN disks may be gravitationally lensed by the supermassive black hole at the AGN centre. The probability of such lensing events has been approximately estimated by using the Einstein criterion in previous work. However, a more reasonable approach to calculating the lensing probability should be based on whether the detector can distinguish the lensed GW waveform from the unlensed one. In this work, we calculate the lensing probability of LIGO sources embedded in AGN disk by relating threshold mismatch to the signal-to-noise ratio of the observed events. For the sensitivity of LIGO-Virgo-KAGRA O3 observation runs, our results indicate that the lensing probability is several times higher than previous estimates. If AGNs are indeed the primary formation channel for BBHs, we could quantify the probability of detecting the lensed GW events in such a scenario. The non-detections, on the other hand, will place stricter constraints on the fraction of AGN disk BBHs and even the birthplaces of BBH mergers.

## I. INTRODUCTION

In 2015, LIGO detected the first binary black hole (BBH) merger event, known as GW150914 [1–3]. Two years later, another significant event was observed – the merger of a binary neutron star, GW170817 [4]. This event was accompanied by the electromagnetic counterpart of GRB170817A [5, 6] and Kilonova AT 2017gfo/DLT17ck [7]. Gravitational waves (GWs) from two neutron star–black hole coalescences were also observed in January 2020 [8]. Up to date, about 90 confident GW detections have been made by LIGO-Virgo-KAGRA (LVK) [9–13]. As the number of detected GW events continues to rise, the formation channels of compact binary systems and the physical mechanisms behind these mergers have extensively studied.

BBHs can form, evolve and merge in the densest environments of AGNs [14–18]. Stellar-mass black holes in AGNs will become gravitationally bound to one another due to the effects of gaseous dynamical friction from the disk [19–28] or stellar dynamical friction from the nuclear star cluster [29]. Stars [30, 31], star clusters [32, 33] and BBHs that are orbiting around the central SMBH may interact with the AGN disk and captured by it, thereby forming potential populations of GW or tidal disruption events [34–36]. These objects embedded within the disk may sink to the so-called migration trap region [37–40] and form BBHs. Some of them may form a hierarchical triple system with the central supermassive black hole (SMBH) and merge in the manner of Kozai–Lidov mechanism [41, 42].

Previous work obtained a significant merger rate of BBHs on the AGN disk through Monte Carlo simulations [43]. A natural consideration is that the GW from BBH mergers can be lensed by the SMBH when the BBH is located behind the SMBH. Inspecting the lensing probability and comparing with the detection results of lensed GW events could put strong constraint on the number of such systems and the merger sites of BBH in the disk.

For such a BBH+SMBH lensing system, the criterion is often approximately characterized by the Einstein radius  $\theta_{\text{Ein}}$  in previous work [44, 45]. [45] find that, with  $\sim 100$  observations, the lensing probability of observing at least one GW 190521-like is about 14%. However, a more reasonable approach to calculating the lensing probability should be based on whether the detector can distinguish the lensed GW waveform from the unlensed one [46–50]. The criterion should depend on the sensitivity of the detector and the SNR of the detected GW events. In this work, we calculate the lensing probability of LIGO sources embedded in AGN disk by relating threshold mismatch to the SNR.

This paper is organized as follows. In Section II, we present our model. In Section III, we present our results on the mismatch arising from gravitational lensing and the lensing probability. Conclusions and discussions are given in Section IV.

## II. GRAVITATIONAL LENSING OF BBH MERGERS IN AGN DISK AND MISMATCHES

The geometric configuration of the gravitational lensing effect of the GW adopted in this work is depicted in Figure 1 (a). Here, the source is the BBH, which is orbiting the SMBH that is considered as the lensing object  $L$ .

<sup>a</sup> hli@lanl.gov

<sup>b</sup> leiwh@hust.edu.cn

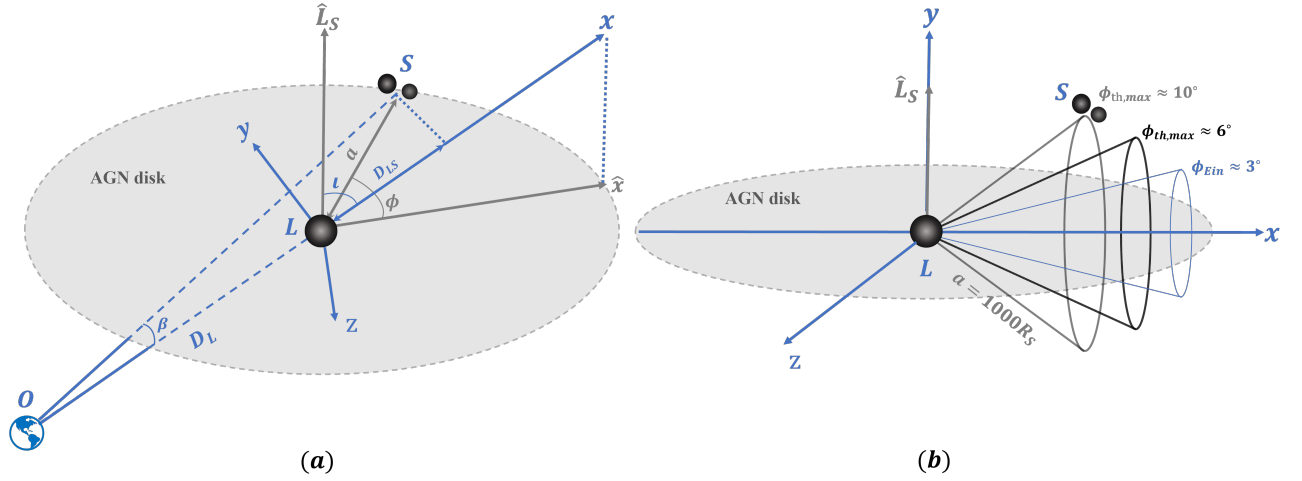


FIG. 1: Schematic diagram of the lensing system. Figure 1 (a) showing a BBH (Source  $S$ ) orbiting an SMBH (Lens object  $L$ ). The gray-shaded region indicating the orbital plane of the source. When the BBHs are located in the conical region on the right, they will form a lensing system with the central SMBH and the observer  $O$  on the left.  $D_L$ ,  $D_S$  and  $D_{LS}$  represent the distance from the observer to lens, the observer to source and the lens to source, respectively.  $\beta$  is the angular position of the source. The position of the source in the disk is represented by  $\phi$ ,  $\iota$ , and  $a$ , where  $\phi$  denotes the orbital phase,  $\iota$  indicates the angle between the source's orbital angular momentum ( $\hat{L}_S$ ) and optical axis ( $x$ -axis), while  $a$  represents the semi-major axis of the source's orbit. Several cones with opening angles of  $\phi_{th,max}$  are also plotted to depict the scenario when lensing of GW will likely occur. We get Figure 1(b) by setting  $\iota = 90^\circ$ .  $\phi_{th,max} \approx 6^\circ$  and  $10^\circ$  corresponds to the maximum threshold orbital phase when the SNR are 8 and 15. The blue solid angle of  $\phi_{Ein} \approx 3^\circ$  is given by Einstein criterion.

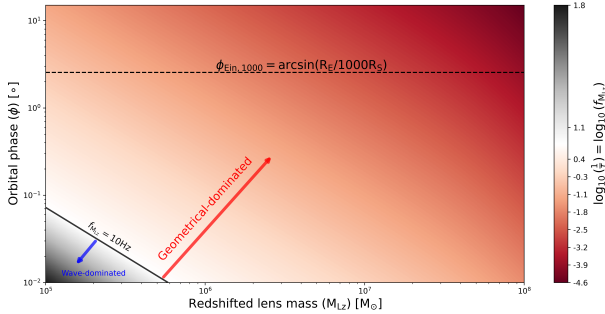


FIG. 2: Contour plot of the characteristic frequency,  $f_{MLz}$ . Wave-optics dominated zone: bottom left region, where  $f_{GW} \sim f_{MLz}$ . The frequency  $f_{MLz} = 10$  Hz corresponds to the lower limit of the LIGO-Virgo sensitivity band. Geometrical-optics zone: upper right region, where  $f_{GW} \gg f_{MLz}$ . For reference, we have plotted the Einstein criterion determined phase angles  $\phi_{Ein,1000}$  in dashed black line, when  $\iota = 90^\circ$ . As seen from the dashed black line in the figure, the Einstein criterion related orbital phase fall entirely within the geometric optics limit.

The reference frame ( $x, y, z$ ) considered here is centered on the lensing object  $L$ . The  $x$ -axis is defined by the line of sight between the observer and the lensing object  $L$ . The  $x$ - $y$  plane is defined by the plane containing both the  $x$ -axis and the source's orbital angular momentum vector

$\hat{L}_S$  around the object  $L$  [47, 51, 52], the angle between the  $y$ -axis and  $\hat{L}_S$  is  $90^\circ - \iota$ . The source location can thus be written as

$$\begin{cases} x(a, \phi, \iota) = a \cos \phi \sin \iota, \\ y(a, \phi, \iota) = a \cos \phi \cos \iota, \\ z(a, \phi) = -a \sin \phi, \end{cases} \quad (1)$$

where  $a$  is the semi-major axis of the source,  $\phi$  is the orbital phase of the source and  $\iota$  is the inclination angle between the line of sight and the orbital angular momentum of the source  $\hat{L}_S$ , with  $\cos(\iota) = \mathbf{x} \cdot \hat{L}_S$ , respectively. From Figure 1 (a), Equations (1) and (3), we can see that the angular source position  $\beta$  is determined by  $a, \phi, \iota$ . Specifically, when  $\iota = 0^\circ$ , this corresponds to a face-on disk. The angular position of the source is  $\beta = a/D_L$ , independent of the source's orbital phase  $\phi$ , and the lensing effect disappears in such a configuration. On the other hand, for a perfectly aligned lensing system, we will have  $\iota = 90^\circ$ ,  $\phi = 0^\circ$  and  $\beta = 0^\circ$ . The dimensionless angular source location of point mass lens model [53] can be expressed as

$$\eta(a, \phi, \iota) = \frac{\beta(a, \phi, \iota)}{\theta_{Ein}(a, \phi, \iota)}, \quad (2)$$

where

$$\beta(a, \phi, \iota) = \frac{\sqrt{y^2(a, \phi, \iota) + z^2(a, \phi, \iota)}}{D_L} \quad (3)$$

is the angular position of the source, and

$$\theta_{\text{Ein}}(a, \phi, \iota) = \sqrt{2R_S \frac{D_{\text{LS}}(a, \phi, \iota)}{D_L D_S}} \quad (4)$$

is the angular Einstein radius with  $D_{\text{LS}} = x(a, \phi, \iota)$  and  $R_S = 2GM_{\text{Lz}}/c^2$  is the Schwarzschild radius of the lens with mass  $M_{\text{Lz}}$ . The time delay between these two images is expressed as

$$\Delta t(a, \phi, \iota, M_{\text{Lz}}) = \frac{4GM_{\text{Lz}}}{c^3} \left[ \frac{\eta(a, \phi, \iota) \sqrt{\eta^2(a, \phi, \iota) + 4}}{2} + \ln \left( \frac{\sqrt{\eta^2(a, \phi, \iota) + 4} + \eta(a, \phi, \iota)}{\sqrt{\eta^2(a, \phi, \iota) + 4} - \eta(a, \phi, \iota)} \right) \right]. \quad (5)$$

Their magnifications are

$$\mu_{\pm}(a, \phi, \iota) = \frac{1}{2} \pm \frac{\eta^2(a, \phi, \iota) + 2}{2\eta(a, \phi, \iota) \sqrt{\eta^2(a, \phi, \iota) + 4}}. \quad (6)$$

Following [54] and [52], the transmission factor of wave optics solution that depends on coordinate parameters have the form of

$$F(f, a, \phi, \iota, M_{\text{Lz}}) = \exp \left\{ \frac{\pi w}{4} + i \frac{w}{2} \left[ \ln \left( \frac{w}{2} \right) - 2\phi_m(\eta) \right] \right\} \times \Gamma \left( 1 - i \frac{w}{2} \right) {}_1F_1 \left( i \frac{w}{2}, 1; i \frac{w\eta^2}{2} \right), \quad (7)$$

where  $\Gamma$  is complex gamma function,  ${}_1F_1$  is confluent hypergeometric function of the first kind, and

$$w(f, M_{\text{Lz}}) = \frac{8\pi G M_{\text{Lz}} f}{c^3} \quad (8)$$

is the dimensionless frequency.  $\phi_m(a, \phi, \iota)$  is defined as

$$\phi_m(a, \phi, \iota) = \frac{1}{2} [\eta_m(a, \phi, \iota) - \eta(a, \phi, \iota)]^2 - \ln [\eta(a, \phi, \iota)], \quad (9)$$

where

$$\eta_m(a, \phi, \iota) = \frac{1}{2} \{ \eta(a, \phi, \iota) + [\eta^2(a, \phi, \iota) + 4]^{1/2} \}. \quad (10)$$

In the geometrical optics limit ( $w \gg 1$ ), we have

$$F(f, a, \phi, \iota, M_{\text{Lz}}) = |\mu_+(a, \phi, \iota)|^{1/2} - i |\mu_-(a, \phi, \iota)|^{1/2} e^{2\pi i f \Delta t(a, \phi, \iota, M_{\text{Lz}})}. \quad (11)$$

Following [55], we use the relation  $f_{M_{\text{Lz}}} \equiv 1/\Delta t$  to determine which region of the parameter space—Geometrical-optics regime, wave-dominated zone, or long-wavelength regime—our sources reside in. Following [48], we make a smooth connection from wave optical solution (see Equation (7)) to geometrical optic limits (i.e. Equation (11)).

For a given unlensed waveform template  $h_{\text{UL}}(f)$ , the lensed waveform  $h_{\text{L}}(f)$  is defined as the product of the transmission factor and the unlensed waveform, as

$$h_{\text{L}}(f, a, \phi, \iota, M_{\text{Lz}}) = F(f, a, \phi, \iota, M_{\text{Lz}}) h_{\text{UL}}(f). \quad (12)$$

The match ( $\mathcal{M}$ ) between these two waveforms provides a method to quantify their similarity, which has the value from zero to unity [56, 57]. The match between lensed and unlensed waveforms are

$$\mathcal{M}(h_{\text{UL}}, h_{\text{L}}) = \max_{\phi_0, \iota_0} \frac{\langle h_{\text{L}} | h_{\text{UL}} \rangle}{\sqrt{\langle h_{\text{L}} | h_{\text{L}} \rangle \langle h_{\text{UL}} | h_{\text{UL}} \rangle}}, \quad (13)$$

where

$$\langle h_{\text{L}} | h_{\text{UL}} \rangle \equiv 2 \int \frac{\tilde{h}_{\text{L}}^*(f) \tilde{h}_{\text{UL}}(f) + \tilde{h}_{\text{L}}(f) \tilde{h}_{\text{UL}}^*(f)}{S_n(f)} df \quad (14)$$

is the noise weighted inner product between lensed and unlensed waveforms, with  $S_n(f)$  as the one-sided noise power spectral density. As a result, the difference between the lensed and unlensed waveforms is represented by

$$\epsilon(f, a, \phi, \iota, M_{\text{Lz}}) = 1 - \mathcal{M}. \quad (15)$$

The mismatch threshold  $\epsilon_{\text{th}}$  is used to determine whether the two waveforms can be distinguished [49, 56, 58–60],

$$\epsilon_{\text{th}}(f, a, \iota, M_{\text{Lz}}; \phi_{\text{th}}) = \frac{1}{\langle h_{\text{L}} | h_{\text{L}} \rangle + \langle h_{\text{UL}} | h_{\text{UL}} \rangle} \simeq \frac{1}{2\rho^2}. \quad (16)$$

where parameter  $\phi_{\text{th}}$  represents the threshold orbital phase corresponding to the mismatch threshold  $\epsilon_{\text{th}}$ , and  $\rho$  is SNR. For a lensing event with a typical detection of  $\rho = 10$ , this means that  $\epsilon \geq \epsilon_{\text{th}} = 0.005$  is an acceptable mismatch to indicate the difference between the lensed and unlensed. Therefore, we may use Equation (16) to estimate the lensing probability.

### III. MISMATCH AND LENSING PROBABILITY

#### A. Mismatch Arising from Lensing

In this section, we calculate the mismatch arising from the gravitational lensing effect, and estimate the lensing probability by using mismatch threshold  $\epsilon_{\text{th}}$ .

A schematic illustration of the lensing system is shown in Figure 1 (a). As indicated by Equation (15), the mismatch is determined by parameters  $a$ ,  $\phi$  and  $\iota$ . The parameter ranges adopted in our analysis are as follows:  $a \in [500 R_S, 5000 R_S]$ ,  $\phi \in [-15^\circ, 15^\circ]$  and  $\iota \in [75^\circ, 105^\circ]$ . We employ the PyCBC python package to compute the mismatch between the lensed waveform and the corresponding unlensed template waveform [61, 62]. The GW strain signals are generated using the IMR-PhenomD waveform model developed by the LVK collaboration [63–65], representing a  $20M_\odot + 20M_\odot$  binary black hole (BBH) merger that encompasses the

full inspiral, merger, and ringdown phases; other parameters are set to their default values. We adopt the aLIGOaLIGOO3LowT1800545 power spectral density (PSD) [11] to represent the LVK's O3 observing run, and the aLIGOAdVO4IntermediateT1800545 PSD [61] for the anticipated O4 run.

The calculated mismatch is shown in Figure 3, where we fix the semi-major axis to be  $a = 500R_S$  (left panel) and  $a = 5000R_S$  (right panel), and set the black hole mass to  $10^8 M_\odot$ . We investigate how the mismatch varies with inclination angle  $\iota$  and orbital phase  $\phi$ . It can be seen that the regions exhibiting significant differences between the lensed and unlensed waveforms are concentrated in a central circular area, corresponding to the well-aligned configurations. According to Equation (16), the SNR of the GW source determines whether the detector can distinguish between the lensed and unlensed waveforms, and thus affects the mismatch threshold. Based on this, we mark the contours corresponding to SNR values of 5, 6, 7, 8, and 9 with black circles in the plot. As the SNR increases from 5 to 9, the parameter space where the lensing effect can in principle be distinguished also expands. The dash-dotted red circular contour in the figure corresponds to  $\epsilon_{\text{th}}$  at an SNR of 4. This corresponds to a threshold orbital phase of  $\phi_{\text{th}} = 4.55^\circ$ . The dotted red circular contour represents  $\epsilon_{\text{th}}$  at an SNR of 10, corresponding to a threshold orbital phase of  $\phi_{\text{th}} = 9.72^\circ$ . The solid red circular marks the Einstein radius. It is seen that the lensing region determined by the mismatch threshold is generally larger than the Einstein radius. The SNR governs the distinguishable parameter space between lensed and unlensed waveforms, with higher SNR values corresponding to broader regions of resolvable differences. The intersection points between the vertical solid white line and the horizontal lines (solid, dashed, and dotted) indicate the maximum values of  $\phi_{\text{th}}$  when  $\iota = 90^\circ$  (the maximum threshold orbital phase is denoted as  $\phi_{\text{th,max}}$ ). Taking into account the symmetry of the point-mass lens, we will use these values to estimate the effective area in parameter space where lensing events may occur. The right panel of Figure 3 shows the case with a semi-major axis of  $a = 5000R_S$ , with all other parameters set identically. It is evident that increasing the semi-major axis significantly reduces the region where lensing may occur. The influence of the semi-major axis and orbital phase on the mismatch is shown in Figure (4)

Similar to Figure 3, we fix  $\iota = 90^\circ$  and set the mass of the SMBH to  $10^8 M_\odot$ , and compute the variation of the mismatch threshold as a function of the semi-major axis and the orbital phase. The results are shown in Figure 4. It can be seen that, on the one hand, the region where the lensing effect is significant is concentrated around  $\phi = 0^\circ$ . As the range of  $\phi$  extends outward from  $0^\circ$  towards both sides of the axis, the BBH gradually deviates from the line of sight, resulting in the decrease of mismatch. On the other hand, as the semi-major axis increases from  $500R_S$  to  $5000R_S$ , the  $\phi_{\text{th}}$  (related to  $\epsilon_{\text{th}}$ ) range in which the lensing effect is prominent gradually shrinks. This

is because when  $\iota = 90^\circ$ , this corresponds to an edge-on disk. The angular position of the source is

$$\beta = a \sin \phi / D_L, \quad (17)$$

and the dimensionless angular position of the source is

$$\eta = \sqrt{\frac{1}{2} r \tan \phi \sin \phi}, \quad (18)$$

in this configuration, where  $r = a/R_S$ . It is apparent that a larger semi-major axis imposes stricter geometric constraints on the system, reducing the available parameter space in exchange for the same lensing features (see Equation 18). As expected, the distinguishable lensing region in the right panel is smaller than that in the left panel. The contour lines in Figure 4 carry the same meaning as the corresponding line styles in Figure 3.

If we assume that the AGN disk is circular with an inclination angle of  $90^\circ$ , then, combined with the symmetry of the point-mass lens potential, rotating the AGN disk around the line of sight once would bring all GW sources with orbital phases smaller than  $\phi_{\text{th,max}}$  into configurations where lensing characteristics are distinguishable. The parameter  $\phi_{\text{th,max}}$  defines a spherical cap centered on the SMBH at the core of the AGN. We have illustrated the geometric configuration of this spherical cap in Figure 1 (b). Based on this geometry, we define the lensing probability as the ratio of the solid angle of the spherical cap to the total solid angle  $4\pi$ . The solid angle of the spherical cap is given by [66]

$$\omega = 2\pi(1 - \cos \phi_{\text{th,max}}). \quad (19)$$

The lensing probability therefore takes the form

$$p(\text{lensing}|\phi_{\text{th,max}}) = \frac{1}{2}(1 - \cos \phi_{\text{th,max}}). \quad (20)$$

## B. Lensing Probability

In previous work, the Einstein radius is employed as a criterion (as the threshold) to evaluate the significance of lensing effects, serving as a boundary for calculating the probability of lensing events occurring [44, 45, 67]. In this simple estimation, the Einstein criterion requires that  $\beta \leq \theta_{\text{Ein}}$ . From Equations (4) and (17), this leads to the inequality  $r \cos^2 \phi_{\text{Ein}} + 2 \cos \phi_{\text{Ein}} - r \geq 0$ . Solving this inequality yields the threshold orbital phase corresponding to the Einstein criterion:  $\phi_{\text{Ein}} = \arccos(\sqrt{r^2 + 1} - 1)/r$ . Substituting this result into Equation (20), and defining  $x = (\sqrt{r^2 + 1} - 1)/r$ , we obtain  $p(\text{lensing}|r) = (1 - x)/2$ , which resembles the result of Equation (A15) in [45]. For the purpose of comparison with our results. The orbital phase distribution related to the Einstein criterion as a function of semi-major axis is shown as a blue dashed line in Figure 5. A schematic illustration of the solid angle defined by the Einstein criterion is also shown in Figure 1 (b). The probability distribution related to the Einstein

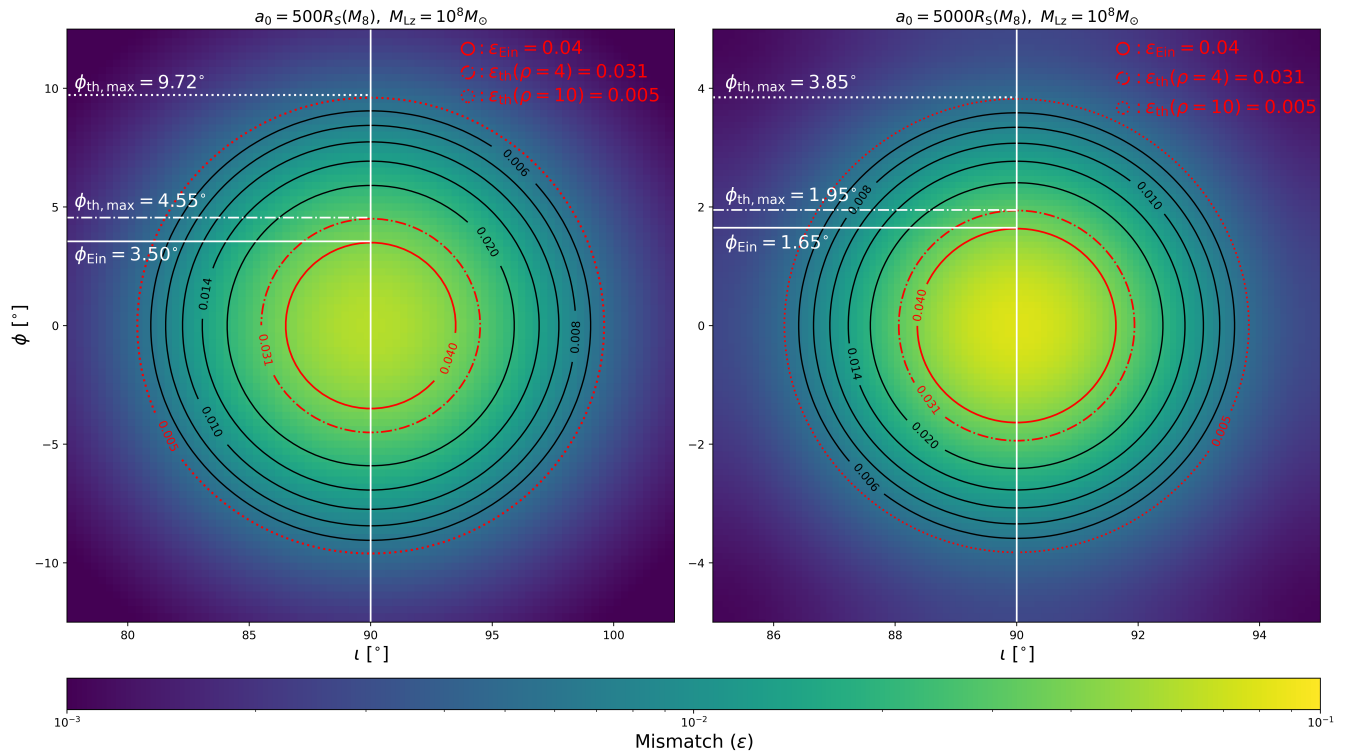


FIG. 3: Contour plot of the mismatch between lensed and unlensed waveform templates as a function of inclination angle and orbital phase. The solid black circle line represents mismatch values for SNR of 5, 6, 7, 8 and 9, with  $M_{LZ} = 10^8 M_\odot$  and  $a_0 = 500R_S(M_8)$  (left) or  $a_0 = 5000R_S(M_8)$  (right). *Left:* The red solid circle line indicates the mismatch corresponding to the Einstein criterion, while the red dashed-dotted circle line shows the mismatch threshold for the minimum SNR of 4. The red dotted circle line represents the threshold for the maximum SNR of 10. The white solid horizontal line corresponds to the orbital phase at the Einstein criterion for  $\iota = 90^\circ$ ,  $a_0 = 500R_S(M_8)$  and  $M_{LZ} = 10^8 M_\odot$ . The white dashed-dotted horizontal line marks the minimum orbital phase for SNR = 4, and the white dotted horizontal line represents the maximum orbital phase for SNR = 10, both for  $\iota = 90^\circ$ ,  $a_0 = 500R_S(M_8)$  and  $M_{LZ} = 10^8 M_\odot$ . *Right:* The right panel is obtained by increasing the semi-major axis from  $500R_S(M_8)$  (left panel) to  $5000R_S(M_8)$ , with all other parameters kept identical.

criterion as a function of semi-major axis is illustrated by the blue dashed line in Figure 6.

However, the Einstein radius serves only as an approximate boundary for the lensing effect. Further study indicates that the effective lensing region is generally larger than the Einstein radius [68, 69]. [60] indicates that the distinguishability of two GW waveforms is determined by the SNR, which in turn depends on the sensitivity of the detector. As seen from Equation (16), a higher SNR results in a smaller mismatch threshold. This implies that, even though there may be only slight differences between the template waveform and the lensed waveform, we may still have the opportunity to distinguish them through matched filtering for sources with a high SNR.

In the following, we employ Equation (20) to evaluate the lensing probability. Among the 93 sources observed by LVK to date [9–13], only two of them have an SNR below 5, one source has an SNR greater than 30, and the majority of sources have an SNR exceeding 10. Based on this observational fact, we select two typical values of the SNR as 8 and 15, which related

to the mismatch threshold of  $\epsilon_{\text{th}} \approx 0.008$  and  $\epsilon_{\text{th}} \approx 0.002$ . For the case with a SNR of  $\approx 8$  (and therefore  $\epsilon_{\text{th}} \approx 0.008$ ), we utilize aLIGOaLIGOO3LowT1800545 [11] as our power spectral density (PSD), and employ aLIGOAdVO4IntermediateT1800545 [61] as our PSD for SNR  $\approx 15$  (and therefore  $\epsilon_{\text{th}} \approx 0.002$ ). For the lens parameters, we chose an edge-on disk ( $\iota = 90^\circ$ ). The semi-major axis of the source ranges from  $500R_S(M_{LZ})$  to  $2000R_S(M_{LZ})$ . Based on these parameters, we calculated the mismatches for  $\epsilon_{\text{th}}(\rho = 8) = 0.008$  and  $\epsilon_{\text{th}}(\rho = 15) = 0.002$  and their related mismatch threshold orbital phase, respectively.

The relationship between the orbital phase  $\phi_{\text{th,max}}$  and semi-major axis  $a$  is shown in Figure 5. The relationship between  $\phi_{\text{th,max}}$  and  $a$  follows a power law of  $\phi_{\text{th,max}} \propto a^{-1/2}$ . As expected,  $\phi_{\text{th,max}}$  gets smaller when  $a$  increases. In Figure 1 (b), we illustrate the cone angles corresponding to the maximum threshold orbital phase derived from the mismatch at  $1000R_S$ , as well as the cone angles corresponding to the Einstein criterion. The cone angle represented by the black solid line and gray solid

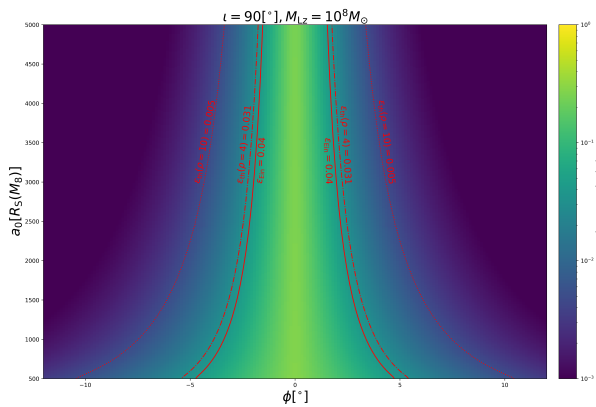


FIG. 4: The mismatch  $\epsilon$  between lensed and unlensed waveform templates as a function of semi-major axis and threshold orbital phase  $\phi_{\text{th}}$ . The red solid line indicates the mismatch corresponding to the Einstein criterion, while the red dashed-dotted line shows the mismatch threshold for the minimum SNR of 4. The red dotted line represents the threshold for the maximum SNR of 10.  $\iota = 90^\circ$  and  $M_{\text{Lz}} = 10^8 M_\odot$  are adopted here.

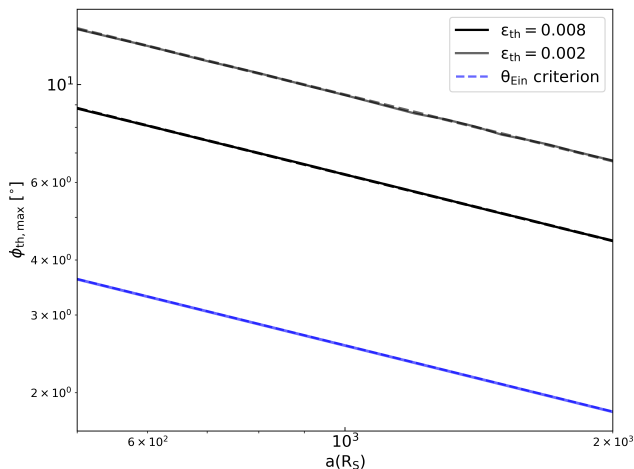


FIG. 5: The  $\phi_{\text{th,max}}$  distribution as a function of semi-major axis  $a$  with  $\epsilon_{\text{th}} = 0.002$  and  $0.008$ . All of the three lines are set  $a = 1000 R_S$  and  $\iota = 90^\circ$ . The blue dashed line represents the Einstein criterion, which relates to the results of [45]. The blue solid line, black dashed line and gray dashed line are the power law fitting result of  $\phi_{\text{th,max}} \propto a^{-1/2}$ .

line corresponds to mismatch values of  $\epsilon_{\text{th}} = 0.008$  and  $\epsilon_{\text{th}} = 0.002$ , respectively, while the cone angle in blue solid line is given by the Einstein criterion. Their corresponding probability distributions are given by Equation (20), as shown in Figure 6. The black solid line represents the case of  $\epsilon_{\text{th}} = 0.008$ , the gray solid line represents the case of  $\epsilon_{\text{th}} = 0.002$ , while the blue dashed line represents the Einstein criterion (equivalent to the mismatch

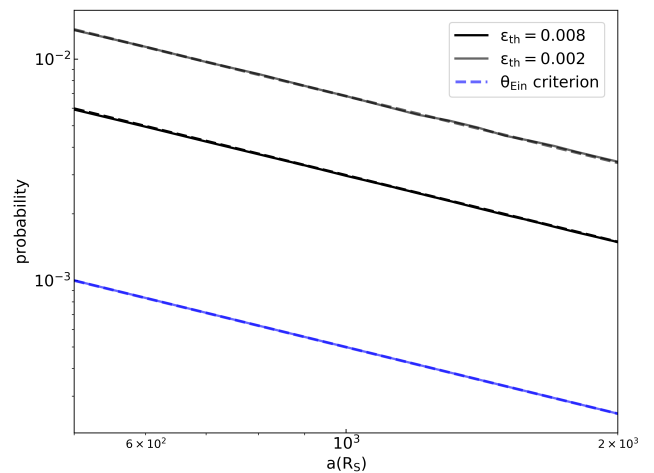


FIG. 6: The lensing probability distribution as a function of semi-major axis  $a$  with  $\epsilon_{\text{th}} = 0.002$  for  $\rho = 15$  and  $0.008$  for  $\rho = 8$ . All of the parameters are the same as in Figure 5. The blue dashed line represents the probability given by Einstein criterion, which relates to the results of [45]. The blue solid line, the black dashed line and the gray solid line are the power law fitting results of  $p(\text{lensing}|\phi_{\text{th,max}}) \propto a^{-1}$ .

threshold of  $\epsilon_{\text{Ein}} = 0.06$ , i.e. corresponding to the results of [45]).

Our results indicate that, for  $a = 1000 R_S$ , the threshold orbital phase  $\phi_{\text{th,max}}$  and lensing probability calculated with the mismatch threshold  $\epsilon_{\text{th}} = 0.008$  for  $\rho = 8$  (or  $\epsilon_{\text{th}} = 0.002$  for  $\rho = 15$ ) will be  $\sim 2$  (or  $\sim 3$ ) and  $\sim 6$  ( $\sim 14$ ) times larger than the result with the Einstein criterion, respectively. The relationship between  $p(\text{lensing}|\phi_{\text{th,max}})$  and  $a$  follows a power law of  $p(\text{lensing}|\phi_{\text{th,max}}) \propto a^{-1}$ . For the case of  $a = 500 R_S$ , the orbital phase  $\phi_{\text{th,max}}$  calculated with the mismatch threshold  $\epsilon_{\text{th}} = 0.008$  for  $\rho = 8$  (or  $\epsilon_{\text{th}} = 0.002$  for  $\rho = 15$ ) will be  $\sim 3$  (or  $\sim 4$ ) times larger than the result with the Einstein criterion. We can see that, as the semi-major axis increases, the subthreshold orbital phase decreases. It is found that, if we take the semi-major axis of the source in units of Schwarzschild radius  $R_S$ , the position of the source will not depend on the lens mass.

#### IV. CONCLUSION AND DISKUSSION

In this study, we propose that the detection criterion for gravitational lensing should be based on the PSD of the detector and the SNR of GW sources. We calculated the lensing probability for BBH mergers in AGN disks through systematic analysis of waveform-template mismatches between lensed and unlensed waveform template banks. For the current observational runs, the typical SNR values are  $\sim 8 - 15$ . In these cases, the orbital phase given by the mismatch threshold is  $\sim 2 - 3$  times

larger than previous estimates (i.e., predicted by the Einstein criterion). The lensing probability will be roughly 10 times larger than the previous result.

GW190521 was reported in [70]. Its plausible optical electromagnetic counterpart to a binary black hole merger was reported in [71]. As argued in [45], with the lensing probability given by the Einstein criterion, if assuming that all BBHs are GW190521-like, located in the migration trap at  $a \simeq 331R_S$ , one can find that with  $\sim 100$  GW events, the probability of observing at least one lensed event is 14%. However, this percentage will be  $\sim 60\%$  (or  $\sim 88\%$ ) for the mismatch threshold  $\epsilon_{\text{th}} = 0.008$  ( $\rho = 8$ ) (or  $\epsilon_{\text{th}} = 0.002$  for  $\rho = 15$ ) if adopting our revised lensing probability. On the other hand, the non-detections will place more strict constraints on the fraction of AGN disk BBHs and even the birthplaces of BBH mergers. We might need to comment that our enhanced rate is ideal. In reality, the enhancement factor should be smaller when considering the real detections.

As illustrated by the lensing configuration in Figure 1 (a), when  $\iota = 90^\circ$ , a smaller  $\phi$  corresponds to more pronounced lensing features, making it easier to identify the presence of lensing features. However, in this case, the lensing probability decreases (see Equation (20)). Conversely, as  $\phi$  increases, the lensing features become less significant, but the lensing probability increases. This poses a significant challenge for the identification of lensed GW events. For the case of subthreshold searching [72], the amplitude of the second image is significantly de-magnified. This may lead to an inaccurate parameter estimation of the source [73, 74], and the weaker signal from the second image may be buried in the noise and therefore overlooked [46]. To justify our revised lensing probability, a dedicated subthreshold targeted search for lensing GW should be performed in the future. We stress that this work does not address the identification of lensed gravitational-wave signals. For studies on the identification of lensed GW events, we refer the reader to [55].

GW lensing is also possible for BBHs in a dense star cluster. Therefore, distinguishing the physical origin of BBHs (in a star cluster or AGN disk) through GW lensing alone remains challenging. To further constrain the specific formation channel, one needs to consider the other detectable effects of the surrounding environment on the GW sources.

## ACKNOWLEDGMENTS

We are very grateful to Meng-Ye Wang, Xiang-Li Lei, Hao Wang, Wen-Fan Feng, Xu-Chen Lu, and Bing Zhang for their helpful discussions. This work is supported by the National Key R&D Program of China (Nos. 2020YFC2201400, SQ2023YFC220007), and the National Natural Science Foundation of China under grant 12473012. W.H.Lei. acknowledges support by the science research grants from the China Manned Space

Project with NO.CMS-CSST-2021-B11. The scope of H.L.'s research presented in this article is on the underlying physics and interpretation of the results and was supported by the Laboratory Directed Research and Development program of Los Alamos National Laboratory under project number 20220087DR.

- [1] R. Abbott *et al.* (The LIGO Scientific Collaboration and the Virgo Collaboration), *Physical Review Letters* **116**, 131103 (2016).
- [2] R. Abbott *et al.* (The LIGO Scientific Collaboration and the Virgo Collaboration), *Physical Review Letters* **116**, 061102 (2016).
- [3] R. Abbott *et al.* (The LIGO Scientific Collaboration and the Virgo Collaboration), *Physical Review D* **93**, 122003 (2016).
- [4] R. Abbott *et al.* (The LIGO Scientific Collaboration and the Virgo Collaboration), *Physical Review Letters* **119**, 131103 (2017).
- [5] R. Abbott *et al.* (The LIGO Scientific Collaboration and the Virgo Collaboration), *The Astrophysical Journal Letters* **848**, L12 (2017).
- [6] A. Goldstein, P. Veres, E. Burns, M. S. Briggs, R. Hamburg, D. Kocevski, C. A. Wilson-Hodge, R. D. Preece, S. Poolakkil, O. J. Roberts, C. M. Hui, V. Connaughton, J. Racusin, A. von Kienlin, T. Dal Canton, N. Christensen, T. Littenberg, K. Siellez, L. Blackburn, J. Broida, E. Bissaldi, W. H. Cleveland, M. H. Gibby, M. M. Giles, R. M. Kippen, S. McBreen, J. McEnery, C. A. Meegan, W. S. Paciesas, and M. Stanbro, *apjl* **848**, L14 (2017), [arXiv:1710.05446 \[astro-ph.HE\]](#).
- [7] S. Valenti, D. J. Sand, S. Yang, E. Cappellaro, L. Tartaglia, A. Corsi, S. W. Jha, D. E. Reichart, J. Haislip, and V. Kouprianov, *apjl* **848**, L24 (2017), [arXiv:1710.05854 \[astro-ph.HE\]](#).
- [8] R. Abbott *et al.* (The LIGO Scientific Collaboration, the Virgo Collaboration and KAGRA Collaboration), *The Astrophysical Journal Letters* **915**, L5 (2021).
- [9] R. Abbott *et al.* (The LIGO Scientific Collaboration and the Virgo Collaboration), *Physical Review X* **9**, 031040 (2019).
- [10] R. Abbott *et al.* (The LIGO Scientific Collaboration and the Virgo Collaboration), *Physical Review X* **11**, 021053 (2021).
- [11] R. Abbott *et al.* (LIGO Scientific Collaboration, Virgo Collaboration, and KAGRA Collaboration), *Phys. Rev. X* **13**, 041039 (2023).
- [12] R. Abbott *et al.* (LIGO Scientific Collaboration, Virgo Collaboration, and KAGRA Collaboration), *Physical Review X* **13**, 011048 (2023).
- [13] R. Abbott *et al.* (The LIGO Scientific Collaboration and the Virgo Collaboration), *Phys. Rev. D* **109**, 022001 (2024).
- [14] N. C. Stone, B. D. Metzger, and Z. Haiman, *MNRAS* **464**, 946 (2017), [arXiv:1602.04226 \[astro-ph.GA\]](#).
- [15] H. Tagawa, Z. Haiman, I. Bartos, and B. Kocsis, *APJ* **899**, 26 (2020), [arXiv:2004.11914 \[astro-ph.HE\]](#).
- [16] H. Tagawa, Z. Haiman, and B. Kocsis, *APJ* **898**, 25 (2020), [arXiv:1912.08218 \[astro-ph.GA\]](#).
- [17] C. Rowan, T. Boekholt, B. Kocsis, and Z. Haiman, *MNRAS* **524**, 2770 (2023), [arXiv:2212.06133 \[astro-ph.GA\]](#).
- [18] M. Wang, Y. Ma, and Q. Wu, *MNRAS* **520**, 4502 (2023), [arXiv:2212.05724 \[astro-ph.HE\]](#).
- [19] H. Tagawa and M. Umemura, *APJ* **856**, 47 (2018), [arXiv:1802.07473 \[astro-ph.GA\]](#).
- [20] Y.-P. Li, A. M. Dempsey, S. Li, H. Li, and J. Li, *APJ* **911**, 124 (2021), [arXiv:2101.09406 \[astro-ph.HE\]](#).
- [21] A. M. Dempsey, H. Li, B. Mishra, and S. Li, *APJ* **940**, 155 (2022), [arXiv:2203.06534 \[astro-ph.HE\]](#).
- [22] R. Li and D. Lai, *MNRAS* **517**, 1602 (2022), [arXiv:2202.07633 \[astro-ph.HE\]](#).
- [23] J. Li, A. M. Dempsey, H. Li, D. Lai, and S. Li, *apjl* **944**, L42 (2023), [arXiv:2211.10357 \[astro-ph.HE\]](#).
- [24] S. DeLaurentiis, M. Epstein-Martin, and Z. Haiman, *MNRAS* **523**, 1126 (2023), [arXiv:2212.02650 \[astro-ph.HE\]](#).
- [25] K. Qian, J. Li, and D. Lai, *APJ* **962**, 143 (2024), [arXiv:2310.12208 \[astro-ph.HE\]](#).
- [26] H. Whitehead, C. Rowan, T. Boekholt, and B. Kocsis, *MNRAS* **531**, 4656 (2024), [arXiv:2309.11561 \[astro-ph.GA\]](#).
- [27] A. J. Dittmann, A. M. Dempsey, and H. Li, *APJ* **964**, 61 (2024), [arXiv:2310.03832 \[astro-ph.HE\]](#).
- [28] J. Calcino, A. M. Dempsey, A. J. Dittmann, and H. Li, *APJ* **970**, 107 (2024), [arXiv:2311.13727 \[astro-ph.HE\]](#).
- [29] M. Dodici and S. Tremaine, *APJ* **972**, 193 (2024), [arXiv:2404.08138 \[astro-ph.GA\]](#).
- [30] P. Artymowicz, D. N. C. Lin, and E. J. Wampler, *APJ* **409**, 592 (1993).
- [31] X. Fan, Q. Wu, J. Wu, X. Lei, M. Wang, and F. Li, *APJ* **966**, 222 (2024), [arXiv:2404.00937 \[astro-ph.GA\]](#).
- [32] S. S. Nasim, G. Fabj, F. Caban, A. Secunda, K. E. S. Ford, B. McKernan, J. M. Bellovary, N. W. C. Leigh, and W. Lyra, *MNRAS* **522**, 5393 (2023), [arXiv:2207.09540 \[astro-ph.GA\]](#).
- [33] Y. Wang, Z. Zhu, and D. N. C. Lin, *MNRAS* **528**, 4958 (2024), [arXiv:2308.09129 \[astro-ph.GA\]](#).
- [34] I. Bartos, B. Kocsis, Z. Haiman, and S. Márka, *APJ* **835**, 165 (2017), [arXiv:1602.03831 \[astro-ph.HE\]](#).
- [35] M. MacLeod and D. N. C. Lin, *APJ* **889**, 94 (2020), [arXiv:1909.09645 \[astro-ph.SR\]](#).
- [36] G. Fabj, S. S. Nasim, F. Caban, K. E. S. Ford, B. McKernan, and J. M. Bellovary, *MNRAS* **499**, 2608 (2020), [arXiv:2006.11229 \[astro-ph.GA\]](#).
- [37] J. M. Bellovary, M.-M. Mac Low, B. McKernan, and K. E. S. Ford, *apjl* **819**, L17 (2016), [arXiv:1511.00005 \[astro-ph.GA\]](#).
- [38] A. Secunda, J. Bellovary, M.-M. Mac Low, K. E. S. Ford, B. McKernan, N. W. C. Leigh, W. Lyra, and Z. Sándor, *APJ* **878**, 85 (2019), [arXiv:1807.02859 \[astro-ph.HE\]](#).
- [39] B. McKernan, K. E. S. Ford, H. E. Cook, V. Delfavero, K. Nathaniel, J. Postiglione, S. Ray, and R. O’Shaughnessy, *arXiv e-prints*, [arXiv:2410.16515 \(2024\)](#), [arXiv:2410.16515 \[astro-ph.HE\]](#).
- [40] V. Delfavero, K. E. S. Ford, B. McKernan, H. E. Cook, K. Nathaniel, J. Postiglione, S. Ray, and R. O’Shaughnessy, *arXiv e-prints*, [arXiv:2410.18815 \(2024\)](#), [arXiv:2410.18815 \[astro-ph.HE\]](#).
- [41] Y. Yang, I. Bartos, V. Gayathri, K. E. S. Ford, Z. Haiman, S. Klimentko, B. Kocsis, S. Márka, Z. Márka, B. McKernan, and R. O’Shaughnessy, *Phys. Rev. Lett.* **123**, 181101 (2019), [arXiv:1906.09281 \[astro-ph.HE\]](#).
- [42] V. Gayathri, I. Bartos, Z. Haiman, S. Klimentko, B. Kocsis, S. Márka, and Y. Yang, *apjl* **890**, L20 (2020), [arXiv:1911.11142 \[astro-ph.HE\]](#).
- [43] B. McKernan, K. E. S. Ford, J. Bellovary, N. W. C. Leigh, Z. Haiman, B. Kocsis, W. Lyra, M. M. Mac Low, B. Metzger, M. O’Dowd, S. Endlich, and D. J. Rosen, *APJ* **866**, 66 (2018), [arXiv:1702.07818 \[astro-ph.HE\]](#).
- [44] D. J. D’Orazio and R. Di Stefano, *MNRAS* **474**, 2975

- (2018), [arXiv:1707.02335 \[astro-ph.HE\]](#).
- [45] S. H. W. Leong, J. Janquart, A. K. Sharma, P. Martens, P. Ajith, and O. A. Hannuksela, *apjl* **979**, L27 (2025), [arXiv:2408.13144 \[astro-ph.HE\]](#).
- [46] C. McIsaac, D. Keitel, T. Collett, I. Harry, S. Mozzon, O. Edy, and D. Bacon, *Phys. Rev. D* **102**, 084031 (2020), [arXiv:1912.05389 \[gr-qc\]](#).
- [47] H. Yu and Y. Chen, *Phys. Rev. Lett.* **126**, 021101 (2021), [arXiv:2009.02579 \[gr-qc\]](#).
- [48] R. Bondarescu, H. Ubach, O. Bulashenko, and A. Lundgren, *Phys. Rev. D* **108**, 084033 (2023), [arXiv:2211.13604 \[gr-qc\]](#).
- [49] S. Ali, E. Stoikos, E. Meade, M. Kesden, and L. King, *Phys. Rev. D* **107**, 103023 (2023), [arXiv:2210.01873 \[gr-qc\]](#).
- [50] S. M. C. Yeung, M. H. Y. Cheung, E. Seo, J. A. J. Gais, O. A. Hannuksela, and T. G. F. Li, *MNRAS* **526**, 2230 (2023), [arXiv:2112.07635 \[gr-qc\]](#).
- [51] Y. Fang, X. Chen, and Q.-G. Huang, *APJ* **887**, 210 (2019), [arXiv:1908.01443 \[astro-ph.HE\]](#).
- [52] H. Yu, Y. Wang, B. Seymour, and Y. Chen, *Phys. Rev. D* **104**, 103011 (2021), [arXiv:2107.14318 \[gr-qc\]](#).
- [53] P. Schneider, J. Ehlers, E. E. Falco, P. Schneider, J. Ehlers, and E. E. Falco, *Gravitational lenses as astrophysical tools* (Springer, 1992).
- [54] R. Takahashi and T. Nakamura, *APJ* **595**, 1039 (2003), [arXiv:astro-ph/0305055 \[astro-ph\]](#).
- [55] A. Mishra, A. K. Meena, A. More, and S. Bose, *MNRAS* **531**, 764 (2024), [arXiv:2306.11479 \[astro-ph.CO\]](#).
- [56] C. Cutler and É. E. Flanagan, *Phys. Rev. D* **49**, 2658 (1994), [arXiv:gr-qc/9402014 \[gr-qc\]](#).
- [57] É. É. Flanagan and S. A. Hughes, *Phys. Rev. D* **57**, 4535 (1998), [arXiv:gr-qc/9701039 \[gr-qc\]](#).
- [58] L. S. Finn, *Phys. Rev. D* **46**, 5236 (1992), [arXiv:gr-qc/9209010 \[gr-qc\]](#).
- [59] L. S. Finn and D. F. Chernoff, *Phys. Rev. D* **47**, 2198 (1993), [arXiv:gr-qc/9301003 \[gr-qc\]](#).
- [60] L. Lindblom, B. J. Owen, and D. A. Brown, *Phys. Rev. D* **78**, 124020 (2008), [arXiv:0809.3844 \[gr-qc\]](#).
- [61] A. Nitz and LIGO Scientific Collaboration, in *APS April Meeting Abstracts*, APS Meeting Abstracts, Vol. 2016 (2016) p. K14.001.
- [62] S. A. Usman, A. H. Nitz, I. W. Harry, C. M. Biwer, D. A. Brown, M. Cabero, C. D. Capano, T. Dal Canton, T. Dent, S. Fairhurst, M. S. Kehl, D. Keppel, B. Krishnan, A. Lenon, A. Lundgren, A. B. Nielsen, L. P. Pekowsky, H. P. Pfeiffer, P. R. Saulson, M. West, and J. L. Willis, *Classical and Quantum Gravity* **33**, 215004 (2016), [arXiv:1508.02357 \[gr-qc\]](#).
- [63] A. Nitz, I. Harry, D. Brown, C. M. Biwer, J. Willis, T. Dal Canton, C. Capano, T. Dent, L. Pekowsky, G. S. Cabourn Davies, S. De, M. Cabero, S. Wu, A. R. Williamson, B. Machenschalk, D. Macleod, F. Pannarale, P. Kumar, S. Reyes, dfinstad, S. Kumar, M. Tápai, L. Singer, P. Kumar, veronica-villa, maxtrevor, B. Uday Varsha Gadre, S. Khan, S. Fairhurst, and A. Tolley, *gwastro/pycbc: v2.3.3 release of PyCBC* (2024).
- [64] S. Husa, S. Khan, M. Hannam, M. Pürrer, F. Ohme, X. J. Forteza, and A. Bohé, *Phys. Rev. D* **93**, 044006 (2016), [arXiv:1508.07250 \[gr-qc\]](#).
- [65] S. Khan, S. Husa, M. Hannam, F. Ohme, M. Pürrer, X. J. Forteza, and A. Bohé, *Phys. Rev. D* **93**, 044007 (2016), [arXiv:1508.07253 \[gr-qc\]](#).
- [66] O. Mazonka, *arXiv preprint arXiv:1205.1396* (2012).
- [67] D. J. D’Orazio and A. Loeb, *Phys. Rev. D* **101**, 083031 (2020), [arXiv:1910.02966 \[astro-ph.HE\]](#).
- [68] K.-H. Lai, O. A. Hannuksela, A. Herrera-Martín, J. M. Diego, T. Broadhurst, and T. G. F. Li, *Phys. Rev. D* **98**, 083005 (2018), [arXiv:1801.07840 \[gr-qc\]](#).
- [69] O. A. Hannuksela, K. Haris, K. K. Y. Ng, S. Kumar, A. K. Mehta, D. Keitel, T. G. F. Li, and P. Ajith, *apjl* **874**, L2 (2019), [arXiv:1901.02674 \[gr-qc\]](#).
- [70] R. Abbott, T. D. Abbott, S. Abraham, F. Acernese, K. Ackley, C. Adams, R. X. Adhikari, V. B. Adya, C. Affeldt, M. Agathos, K. Agatsuma, N. Aggarwal, O. D. Aguiar, A. Aich, L. Aiello, A. Ain, *et al.*, *Phys. Rev. Lett.* **125**, 101102 (2020), [arXiv:2009.01075 \[gr-qc\]](#).
- [71] M. J. Graham, K. E. S. Ford, B. McKernan, N. P. Ross, D. Stern, K. Burdge, M. Coughlin, S. G. Djorgovski, A. J. Drake, D. Duev, M. Kasliwal, A. A. Mahabal, S. van Velzen, J. Belecki, E. C. Bellm, R. Burruss, S. B. Cenko, V. Cunningham, G. Helou, S. R. Kulkarni, F. J. Masci, T. Prince, D. Reiley, H. Rodriguez, B. Rusholme, R. M. Smith, and M. T. Soumagnac, *Phys. Rev. Lett.* **124**, 251102 (2020), [arXiv:2006.14122 \[astro-ph.HE\]](#).
- [72] H. Abbott, R. Abe *et al.*, *APJ* **970**, 191 (2024), [arXiv:2304.08393 \[gr-qc\]](#).
- [73] K. K. Y. Ng, K. W. K. Wong, T. Broadhurst, and T. G. F. Li, *Phys. Rev. D* **97**, 023012 (2018), [arXiv:1703.06319 \[astro-ph.CO\]](#).
- [74] T. Broadhurst, J. M. Diego, and I. Smoot, George, *arXiv e-prints*, [arXiv:1802.05273](#) (2018), [arXiv:1802.05273 \[astro-ph.CO\]](#).